Synthesis and Characterization of B-site Doped $La_{0.20}Sr_{0.25}Ca_{0.45}TiO_3$ as SOFC Anode Materials

Azra Yaqub[1,2], Naveed K. Janjua[1], Cristian Savaniu[2], John T.S. Irvine[2]

[1]Department of Chemistry, Quaid-i-Azam University, Islamabad, Pakistan, 45320

[2]School of Chemistry, University of St Andrews, Fife, Scotland, KY16 9ST

Abstract

Doping at A and/or B sites in the perovskites has always remained a strategy to tailor their properties. In this paper, we report B-site doping of an optimized A-site deficient composition, calcium-doped lanthanum strontium titanate, $La_{0.2}Sr_{0.25}Ca_{0.45}TiO_3$ ($LSCT_{A-}$). $LSCT_{A-}$ was doped at B site with Ni (LSCTN) and Fe (LSCTF). The doped compositions were successfully synthesized by the Pechini method and then characterized. The doped analogues exhibited the same orthorhombic symmetry as the parent however an expansion in the unit cell volume was observed, which is in accordance with the ionic sizes of the dopants. The observed dilatometric results were correlated with the particle size. Ac impedance studies revealed their semi-conducting behaviour in air. Measurement of dc conductivity in reducing atmosphere showed the n-type nature. Furthermore, the doped compositions offered higher conductivity values in reducing atmosphere than the pristine. Much higher values of conductivity were observed for pre-reduced samples. Compared to bare pre reduced $LSCT_{A-}$ having conductivity of 38 S cm^{-1}, the pre reduced 5% Ni doped $LSCT_{A-}$ (LSCTN-5) and 5% Fe doped $LSCT_{A-}$ (LSCTF-5) offered conductivity values of 47 S cm^{-1} and 66 S cm^{-1} at 880 ^oC respectively. In conclusion, catalyst introduction via doping could enhance the electrical and catalytic properties of these materials making them viable alternatives for fuel cell applications.

Keywords: B-site doping, Dc conductivity, Anode material, Fuel cell

1. Introduction

The innate limitations of Ni/YSZ have led scientists and researchers to modify Ni/YSZ cermet as well as to explore alternate anode materials for solid oxide fuel cells (SOFCs). In this aspect, Ni/YSZ has been modified by replacing Ni with other metals like Ru or Cu and replacing YSZ with other alternate oxide ion conductors such as ceria stabilized zirconia, calcium-doped ceria, yttria-doped ceria, titania doped yttria stabilized zirconia or samarium doped ceria.

The modification and improvement of metal cermets has resulted in good performance using either hydrogen or methane as the fuel however none of them is as efficient as Ni/YSZ. The metal cermets also suffer from general problems like sintering and volume instability. To reduce the structural mismatch between anode and electrolyte, single phase oxide anodes have been developed. Major attention has been given to mixed ionic and electronic oxides because they result in enhancement of reaction zone over the three phase boundary thereby affecting the reaction kinetics. The anode development for SOFCs has been detailed in various reviews [1-4].

Among single phase oxides, perovskites have gained major interest due to good stability and reasonable electronic conductivity in reducing conditions. The general formula of perovskite oxides is ABO_3 where A and B cations are 6-fold and 12-fold coordinated to the oxygen anions respectively. The structure consists of BO_6 octahedra sharing the corners of the cube containing the A cation at the centre. The A-site is usually occupied by alkaline earth and/or rare earth metal ions while small transition metal ions (usually from 3d series) occupy the B site.

The structure, redox properties, conductivity as well as the electro-catalytic properties of the parent perovskite are largely affected by B site dopants [5]. The B-site network plays its role in electronic conduction in perovskites. The existence of multiple oxidation states of the transition metals at B-site such as Ti, Cr, Mn or Mo facilitate electronic conductivity due to electron hopping from $B^{(n-1)+}$ to B^{n+} cations. Thus, one of the strategies to improve the electrical conductivity is via B-site doping.

In the family of perovskites, titanate-based oxides have good stability and reasonable n-type electronic conductivity in reducing conditions. In reducing conditions, Ti^{+4} reduces to a lower oxidation state accompanied by creation of oxygen vacancies as the lattice oxygen is removed. The electronic charge carriers formed in this process (see the equation below) take part in enhancing the conductivity [6];

$$2Ti_{Ti}^{X} + O_{O}^{X} \rightarrow 2Ti_{Ti}^{/} + V_{O}^{\cdot\cdot} + \frac{1}{2}O_2$$

This behavior makes them attractive as potential anode materials for SOFCs. Among titanates, $SrTiO_3$ has always remained in focus due to its good electronic conductivity in fuel cell conditions and its resistance to sulphur which is one of the limitations of Ni-YSZ cermet anodes. Both A and/or B sites of the strontium titanate have been doped to tune and tailor its properties. Special attention has been given to

enhance its electrical conductivity by partial substitution of Sr^{2+} on A-site and/or Ti^{4+} on B site [7,8].

Recently, John and Ahmed have reported that calcium doping in A-site deficient Lanthanum strontium titanate enhances its electrical conductivity where maximum conductivity was observed for $La_{0.20}Sr_{0.25}Ca_{0.45}TiO_3$ ($LSCT_{A-}$) composition [9]. Furthermore, the same composition was tested as an anode in fuel cell conditions where good performance was achieved [10]. Recently we have reported the solution phase synthesis of $LSCT_{A-}$ [11].

In this work, we investigate the effect of via B-site doping on the conductivity of $LSCT_{A-}$. Fe and Ni have good catalytic activity so they were chosen as B-site dopants. Additionally, the doping level (1% and 5%) was kept low to have good solubility and preservation of dense network of Ti on B-site of perovskite. The doped compositions were synthesized, characterized and investigated for dc conductivity.

2. Experimental

All materials were prepared by modified Pechini method described in detail previously [11]. Room temperature powder X-ray diffraction (XRD) was performed on a Philips XRD diffractometer using Cu-$K\alpha_1$ radiation in the 2θ range of 20^o to 80^o in the reflection mode. Diffraction peaks were fitted with STOE WinXPOW software to calculate the values of lattice parameters. The morphology of the calcined powders was studied using a JEOL 6700F field emission microscope. Sinterability of doped analogues was investigated using a Netzch DIL 402C instrument. For ac. impedance, the pellets were sintered in air at 1400 ^oC for 6 hours and the surface of sintered pellets was polished and coated with Pt paste which was then consolidated at 900 ^oC for one hour. Impedance data were taken using a Solartron 1260 impedance/gain phase analyzer in the frequency range of 1 Hz to 13 MHz. The measured impedance data were analyzed by the Z view program. van der Pauw method was used to measure dc conductivity of the synthesized samples.

Table 1 lists the investigated doped analogues of $LSCT_{A-}$.

Table 1 Studied doped analogues of $LSCT_{A-}$

Doped analogues	Codes

$La_{0.2}Sr_{0.25}Ca_{0.45}Ti_{0.99}Ni_{0.01}O_3$	LSCTN1
$La_{0.2}Sr_{0.25}Ca_{0.45}Ti_{0.95}Ni_{0.05}O_3$	LSCTN5
$La_{0.2}Sr_{0.25}Ca_{0.45}Ti_{0.99}Fe_{0.01}O_3$	LSCTF1
$La_{0.2}Sr_{0.25}Ca_{0.45}Ti_{0.95}Fe_{0.05}O_3$	LSCTF5

3. Results and Discussion

3.1 Crystal Structure of doped samples

Room temperature XRD of as prepared doped analogues show characteristic reflections of perovskite crystal structure shown in Fig. 1. Similar XRD pattern was observed in all compositions and no impurity peak was detected in any of X-ray diffraction patterns showing full solubility of these dopants up to the doping level added. XRD of parent $LSCT_{A-}$ is also given for comparison.

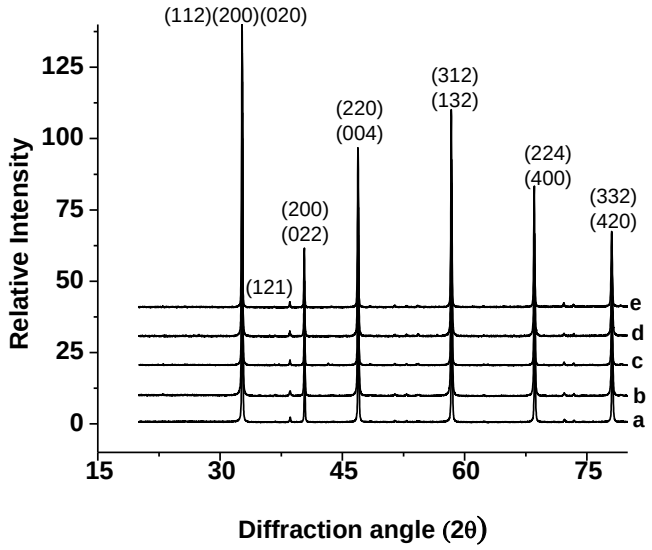

Fig. 1: XRD patterns of doped analogues of $LSCT_{A-}$, a) $LSCT_{A-}$, b) LSCTN1, c) LSCTN5, d) LSCTF1 and e) LSCTF5.

The ionic radii of Fe^{+3}(0.645 Å) and Ni^{+2}(0.690 Å) are greater than the Ti^{+4} (0.605 Å) thus unit cell volume is expected to increase with these dopants. The ionic radii of Ni^{+2} is greater than Fe^{+3} so it is anticipated that Ni^{+2} doping would result in more expansion in unit cell volume. Similar trend was noticed in XRD pattern where

the peaks shifted slightly to low angle theta upon doping. The shifting suggests that Ti^{+4} was successfully substituted by larger Ni^{+2} and Fe^{+3}

The peaks were indexed in orthorhombic symmetry with space group Pbnm using WinXPOW software. An increase in lattice parameters was observed upon doping with Fe and Ni. The variation of lattice parameter *a* in the doped compositions is shown in Fig. 2a where the trend can be explained by considering the ionic sizes of the dopants.

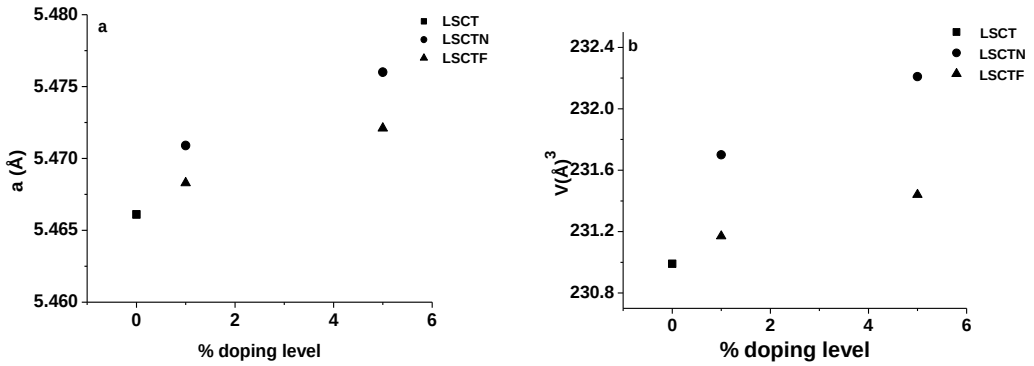

Fig. 2: Variation of lattice parameter *a* (a) and volume (b) of doped analogues of $LSCT_{A-}$.

The unit cell volume is plotted in Fig. 2b. We see that the doping results in an expansion of unit cell. The expansion in volume with Ni^{+2} as dopant is more than Fe^{+3} in accordance with their sizes.

3.2 Morphological Investigation

The SEM micrographs of surfaces of dense pellets of synthesized compositions sintered at 1400 ^{o}C are presented in Fig. 3. The micrographs show well sintered grains with averages size of ~10 micron in diameter with no surface pores. The obtained compact microstructure shows good densification after sintering.

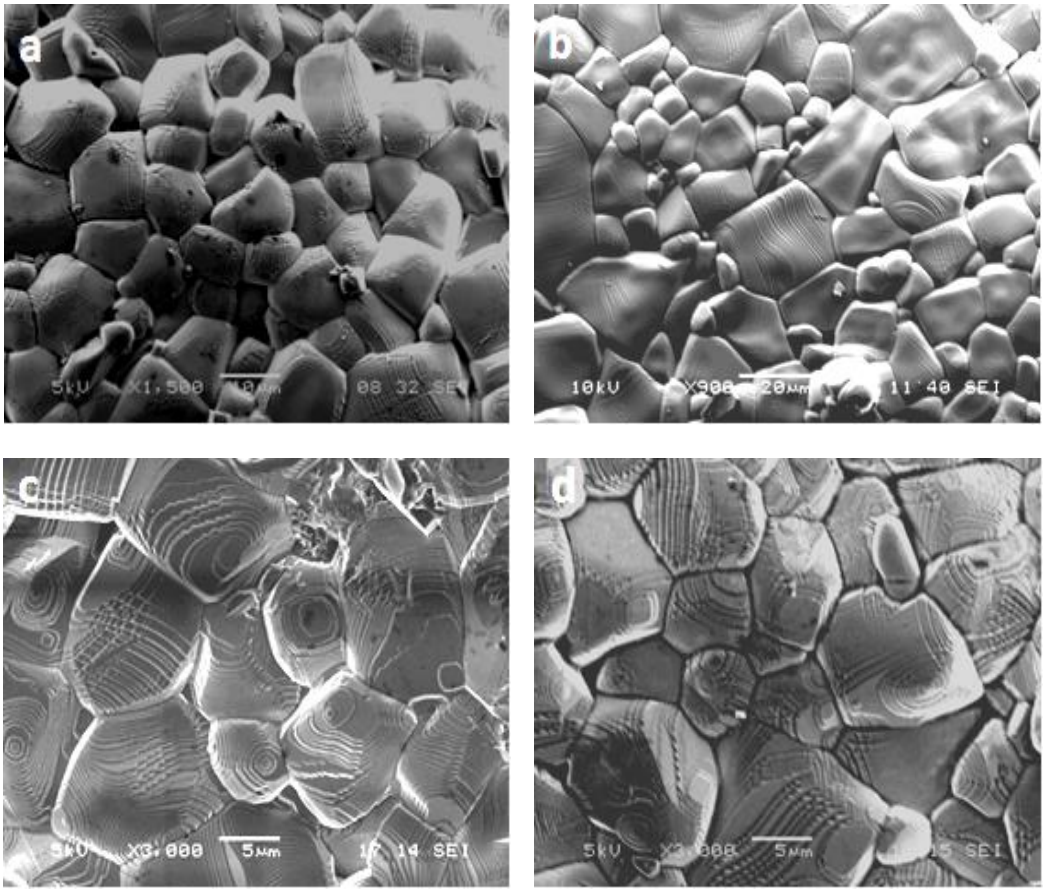

Fig. 3: Micrographs of doped analogues of $LSCT_{A-}$, a) LSCTN1, b) LSCTN5, c) LSCTF1 and d) LSCTF5 after sintering at 1400 ^{o}C for 6 hours in air.

3.3 Sinterability

To avoid thermal mismatch, cracking or de-lamination, thermal expansion compatibility between anode materials and other fuel cell components is essential. Dilatometric investigation of thermal expansion behaviour of doped analogues is shown in Fig. 4.

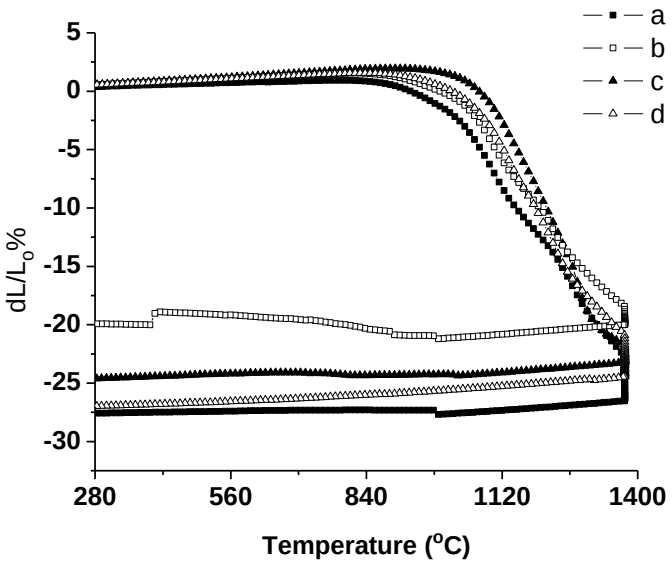

Fig. 4: Dilatometric sintering curves doped analogues of $LSCT_{A-}$ in air; a) LSCTN1, b) LSCTN5, c) LSCTF1 and d) LSCTF5.

The particle size has a pronounced effect on the sintering profile, e.g., small size leads to more sinterability. The % shrinkage calculated from above graph is given in Table 2.

Table 2 Shrinkage percentage of doped analogues in air calculated from dilatometric data

Codes	**% Shrinkage**
LSCTN	26.59
LSCTN5	21.12
LSCTF	25.24
LSCTF5	24.82

The values show that the shrinkage of 5% doped analogues is less compared to 1% doped. The results can be correlated to the respective particle sizes of the calcined powders. The Increase of doping caused increase in particle size which resulted in comparatively less shrinkage of 5% doped analogues. The results also suggest that the thermal shrinkage can be controlled via doping strategy.

3.4 Ac Impedance Studies

The electrical properties of sintered samples with Pt electrodes were investigated by ac impedance in air at various temperatures. The Nyquist plot for LSCTF1 is shown in Fig. 5. It is observed that the resistance decreases with increase in temperature as expected for an electronic semi conductor.

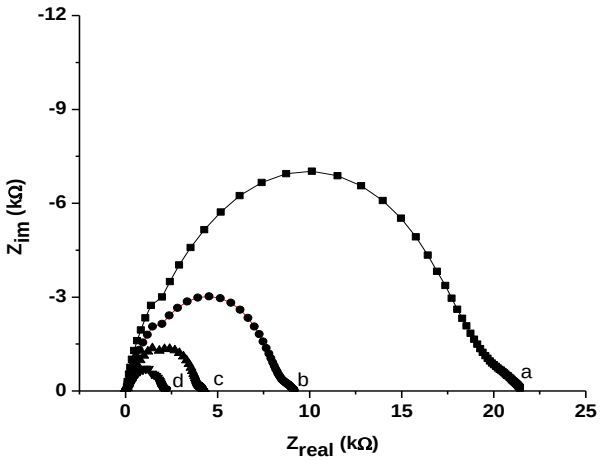

Fig. 5: Cole Cole plots of air sintered LSCTF1 in frequency range of 1 Hz to 13 MHz at different temperatures; a) 600 ^{o}C, b) 650 ^{o}C, c) 700 ^{o}C and d) 750 ^{o}C.

The dependence of real part of Z as a function of frequency at different temperatures for the same sample is shown in Fig. 6a. The impedance-frequency trends merge in the high frequency region irrespective of temperature. This may be due to the release of space charges as a result of reduction in the barrier properties of the material with rise in temperature and may be the responsible factor for the enhancement of ac conductivity of the material with temperature at higher frequencies [12, 13].

Fig. 6b demonstrates the dependence of corresponding imaginary part of impedance on frequency at different temperatures. Distinct peaks appear in impedance spectrum where increase in temperature resulted in asymmetric broadening and decrease in Z″ magnitude due to loss in resistive property of the sample with rise in temperature. The graphs also show the shifting of imaginary Z with increase in temperature. At high frequencies, all the graphs show similar behavior irrespective of temperature [14, 15].

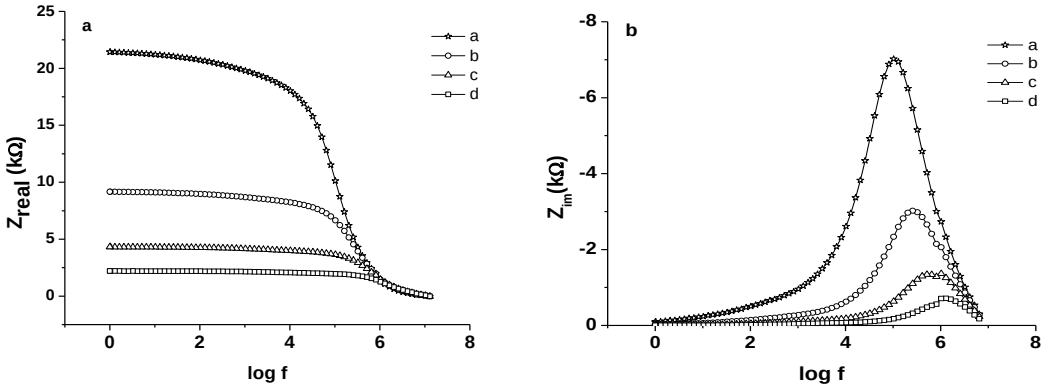

Fig.6: Dependence of real part (a) and imaginary (b) parts of impedance on frequency for air sintered LSCTF1 in frequency range of 1 Hz to 13 MHz in air at different temperatures; a) 600 ^{o}C, b) 650 ^{o}C, c) 700 ^{o}C and d) 750 ^{o}C.

Such results have been attributed to existence of temperature dependent relaxation with a spread of relaxation times in the material. The relaxation species may possibly be immobile species/electrons at low temperature and defects/vacancies at higher temperatures [16, 17]. All the other investigated samples showed similar trend where the resistance decreased with heating showing semi-conducting behavior of the studied compositions.

3.4 Electrical Conductivity

Dc conductivity measurements were conducted on pellets of doped $LSCT_{A}$- samples sintered in air at 1400 ^{o}C. Fig. 7 represents the conductivity –time profile of LSCTN1 in reduced atmosphere ^{o}C maintained by flushing 5% H_2/Ar at 880 ^{o}C. The dc conductivity increases with extent of reduction showing n-type nature.

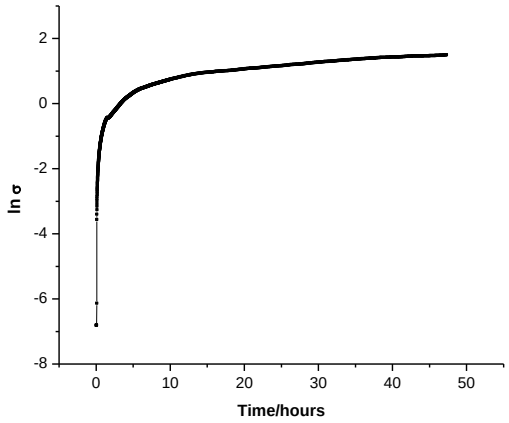

Fig.7: Conductivity profile of in-situ reduced LSCTN1 pellet in 5% H_2/Ar at 880 °C

After an initial delay, the reduction proceeds in two stages, rapidly in the first few hours, followed by a much slower subsequent increase. The equilibrium value could not be reached even after 50 hours of reduction but the increase in conductivity value was gradual as time progressed. These two stages might be related to the fast removal of oxygen from the surface of the perovskite that is followed by a slow diffusion into the bulk of the micron size grains [11, 18, 19].

Similar trends were observed in all other samples. The values of conductivity recorded after 24 hours of in-situ reduction at 880 ^{o}C in each case is tabulated in Table 3.

Table 3: Conductivity of doped analogues upon in-situ reduction in reducing atmosphere (5% H_2/Ar) at 880 ^{o}C

Samples	**Conductivity (S cm^{-1})**
$LSCT_{A-}$	1.30
LSCTN 0.01	2.12
LSCTN 0.05	3.41

LSCTF 0.01	2.99
LSCTF 0.05	4.48

For comparison, the conductivity of $LSCT_{A-}$ is also given. All the doped compositions showed higher conductivity values than the parent. It can also be seen that the conductivity also depends on the dopant level. 5% doping resulted in higher conductivity than 1% doping in case of both iron doped and nickel doped $LSCT_{A-}$. Thus these new compositions can be further tested for anode applications. It is expected that these doped analogues would perform better as anode owing to their better conductivity

The 5% doped samples offering high conductivity (LSCTN5 and LSCTF5) were pre- reduced in reducing atmosphere with 5% H_2/Ar at 1050 ^oC for 24 hours. Then the conductivity-temperature profile was monitored in same atmosphere as shown in Fig. 8.

On cooling, the conductivity increases with the decrease in temperature until ~320 K indicative of positive temperature coefficient of resistance and metallic type behaviour. This suggests electronic conduction to be the pre-dominant mechanism in these materials. Further decrease of temperature from ~320 K to room temperature causes drop of conductivity showing metal insulator transition.

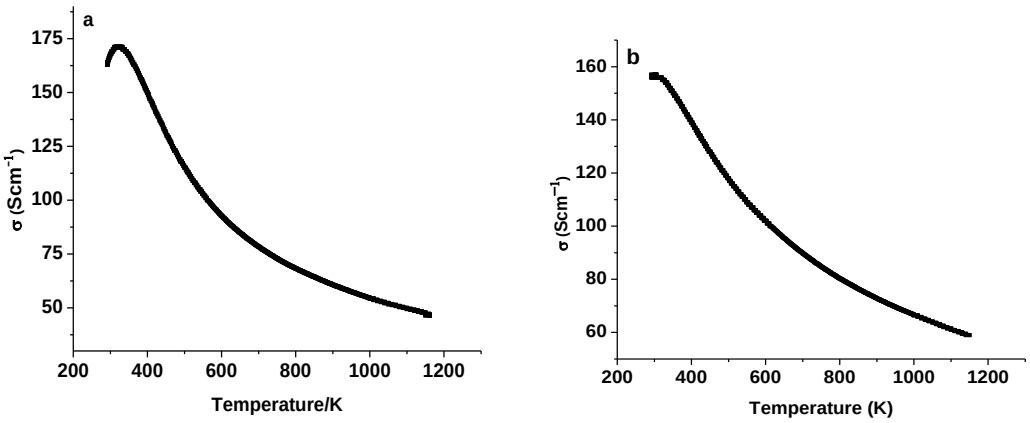

Fig. 8: Conductivity profile during heating of pre reduced samples in reducing atmosphere (5% H_2/Ar); a) LSCTN5 and b) LSCTF5.

From above graphs, the value of conductivity determined at 880 ^oC is tabulated in Table 4.

Table 4 Conductivity of pre-reduced doped analogues in reducing atmosphere (5% H_2/Ar) at 880 ^oC

Samples	**Conductivity (Scm^{-1})**
$LSCT_{A-}$	38.0
LSCTN5	66.1
LSCTF5	46.8

A significant improvement in conductivity of parent composition $LSCT_{A-}$ is observed upon 5% doping with Fe and Ni. The pronounced increase in conductivity values in pre-reduced samples may point to their applications in fuel cells where the reducing atmosphere is an essential environment at the anode site.

The same samples were then tested for morphology. The micrographs show that surface of reduced samples is decorated with small particles which were not present in the sintered samples. The micrographs of pre reduced LSCTF5 and LSCTN5 are shown in Fig. 9.

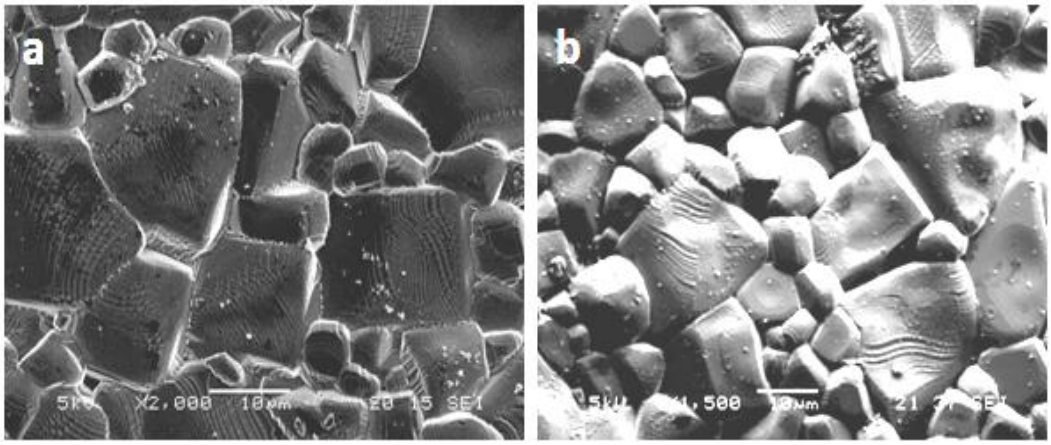

Fig. 9: Micrographs of pre reduced samples; a) LSCTN5 and b) LSCTF5.

.

The exsolution of B-site dopants in perovskites upon reduction has been discussed in the literature [20-23]. From the similar studies carried out earlier, the nature of nano particles can be inferred where Ni was exsolved upon reduction in LSCTN5. Although Fe is comparatively difficult to exsolve [24], however the manipulated defect chemistry is assumed to be responsible for its exsolution (Fig. 9b). The exsolution has been attributed to the inability of the host lattice to accommodate vacancies (A-site vacancies and inherent and introduced oxygen vacancies) beyond a certain limit upon reduction. Thus the defect chemistry provides the driving force for the exsolution of B site dopants.

The proposed mechanism for exsolution involves creation of oxygen vacancies in titanate upon reduction in first step. In the second step, the limit of oxygen vacancies is reached and the perovskite lattice cannot hold any more vacancies. Further reduction results in exsolution of small proportion of B site dopants to surface with simultaneous reduction to the respective metals [24]. Recently, it has been shown that A-site deficiency provides additional driving force for exsolution of nano particles [25].

Among various applications, the metal nano particles precipitation has been shown to improve catalytic properties of the SOFC anodes where the degradation of SOFC anode is successfully eliminated by repeated redox cycling. Upon oxidation, these metal nano particles redissolve in the oxide lattice and subsequent reduction causes precipitation of fresh metal nano particles again available for enhanced performance. This regenerative behaviour of nano particles reduces the anode degradation [26, 27].

The key requirement to prepare such SOFC anodes is to have a catalyst element having good solubility in the lattice in air (at high oxygen partial pressure) and a relatively low free energy of oxide formation so that precipitation of separate metallic phase could take place upon reduction [28].

Thus it is anticipated that these doped analogues would serve to be better anode candidate then parent $LSCT_{A-}$. Nevertheless, further investigations, especially symmetrical and button cell testing are required to evaluate the effect of the Ni and Fe doping on the electrochemical performance of $LSCT_{A-}$.

4. Conclusions

Fe and Ni doped analogues were successfully synthesized via Pechini method with an aim to further improve the conductivity of parent $LSCT_{A-}$. The doped analogues offered better conductivity than the parent imparting these new compositions as suitable anode support candidates. The B-site dopants were ex-solved upon reduction due to manipulation of the defect chemistry of doped compositions. It is inferred that B-site doping is an effective approach to improve the conductivity of the pristine and these doped analogues would be better anode candidate then parent $LSCT_{A-}$.

References

1. S. Tao, J.T.S. Irvine, *Chem. Rec.*, 2004, **4**, 83 – 95.
2. J.W. Fergus, *Solid State Ionics*, 2006, **177**, 1529 – 1541.
3. A. Atkinson, S. Barnett, R.J. Gorte, J.T.S. Irvine, A.J. Mcevoy, M. Mogensen, S.C. Singhal, J. Vohs, *Nature*, 2004, **3**, 17 – 27.
4. J.B. Goodenough, Y.H. Huang, *J. Power Sources*, 2007, **173,** 1 – 10.
5. D.N. Miller, J.T.S. Irvine, *J. Power Sources*, 2011, **96**, 7323 – 7327.
6. P. R. Slater, D. P. Fagg and J.T.S. Irvine, *J. Mater. Chem*., 1997, **7,** 2495–2498.
7. J. Canales-Vazquez, S. W. Tao and J. T. S. Irvine, *Solid State Ionics*, 2003, **159**, 159–165.
8. K. B. Yoo and G. M. Choi, Solid State Ionics, 2009, **180**, 867–871.
9. A. D. Aljaberi and J. T. S. Irvine, *J. Mater. Chem. A*, 2013, **1**, 5868–5874.
10. M. C. Verbraeken, B. Iwanschitz, A. Mai and J. T. S. Irvine, *J. Electrochem. Soc.*, 2012, **159**, F757–F762.
11. A. Yaqub, C. Savaniu, N. K. Janjua, John T. S. Irvine, *J. Mat. Chem. A*, 2013,**1**, 14189-14197.
12. S. Sumi, P.P. Rao, M. Deepa, P. Koshy, *J. App. Phys*., 2010, **108**, 063718 (1 – 9).
13. S. Brahma, R.N.P. Choudhary, A.K. Thakur, *Physica B.*, 2005, **355**, 188 – 201.
14. Z.G. Yi, Y.X. Li, Y. Wang, Q.R. Yin, *J. Electrochem. Soc.*, 2006, **153**, F100 – F105.
15. K. Verma, S. Sharma, *Phys. Status Solidi B.*, 2012, **249**, 209 – 216.
16. R. Rizwana, T.R. Krishna, A.R. James, P. Sarah, *Cryst. Res. Technol*., 2007, **42**, 699 – 706.
17. A.M.M. Farea, S. Kumar, K.M. Batoo, A. Yousef, Alimuddin, *Physica B.*, 2008, **403**, 684 – 701.
18. O.A. Marina, N.L. Canfield, J.W. Stevenson, *Solid State Ionics*, 2002, **149**, 21– 28.
19. D. Neagu, J.T.S. Irvine, *Chem. Mater*., 2010, **22**, 5042 – 5053.
20. Y. Nishihata, J. Mizuki, T. Akao, H. Tanaka, M. Uenishi, M. Kimura, T. Okamoto, N. Hamada, *Nature*, 2002, **418**, 164 – 167.

21. Y. Wang, B. D. Madsen, W. Kobsiriphat, S. A. Barnett and L. D. Marks, *Microsc. Microanal*., 2007, **13**, 100 – 101.
22. D. M. Bierschenk, E. Potter-Nelson, C. Hoel, Y.G. Liao, L. Marks, K.R. Poeppelmeier, S.A. Barnett, *J. Power Sources*, 2011, **196**, 3089 – 3094.
23. B. D. Madsen, W. Kobsiriphat, Y. Wang, L. D. Marks, S. A. Barnett, *ECS Trans*., 2007, **7**, 1339 – 1348.
24. G. Tsekouras, D. Neagu, J.T.S. Irvine, *Energy Environ. Sci*., 2013, **6**, 256 – 266.
25. D. Neagu, G. Tsekouras, D.N. Miller, H. Menard and J. T. S. Irvine, *Nat. Chem.*, 2013, **5**, 916-923.
26. L. Adijanto, V.B. Padmanabhan, R. Kungas, R.J. Gorte, J.M. Vohs, *J. Mater. Chem*., 2012, **22**, 11396 – 11402.
27. W. Kobsiriphat, B.D. Madsen, Y. Wang, L.D. Marks, S.A. Barnett, *Solid State Ionics*, 2009, **180**, 257 – 264.
28. B.D. Madsen, W. Kobsiriphat, Y. Wang, L. D. Marks, S. A. Barnett, *J. Power Sources*, 2007, **166**, 64 – 67.